JCTC Journal of Chemical Theory and Computation

Article

pubs.acs.org/JCTC

Molecule–Lead Coupling at Molecular Junctions: Relation between the Real- and State-Space Perspectives

Tamar Zelovich,[†] Leeor Kronik,[‡] and Oded Hod*[,†]

[†]Department of Chemical Physics, School of Chemistry, The Raymond and Beverly Sackler Faculty of Exact Sciences, Tel Aviv University, Tel Aviv 6997801, Israel

[‡]Department of Materials and Interfaces, Weizmann Institute of Science, Rehovoth 76100, Israel

ABSTRACT: We present insights into the lead–molecule coupling scheme in molecular electronics junctions. Using a "site-to-state" transformation that provides direct access to the coupling matrix elements between the molecular states and the eigenstate manifold of each lead, we find coupling bands whose character depends on the geometry and dimensionality of the lead. We use a standard tight-binding model to elucidate the origin of the coupling bands and explain their nature via simple "particle-in-a-box" type considerations. We further show that these coupling bands can shed light on the charge transport behavior of the junction. The picture presented in this study is not limited to the case of molecular electronics junctions and is relevant to any scenario where a finite molecular entity is coupled to a (semi)infinite system.

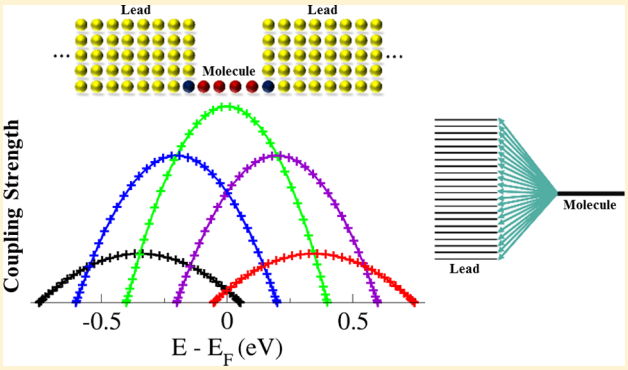

INTRODUCTION

Interfaces between finite molecular entities and extended surfaces are ubiquitous in the field of surface science. Such junctions are of key importance for several new technologies based on organic–inorganic interfaces including fuel cells,[1,2] photovoltaic cells,[3−5] and molecular electronics.[6−9] Here, the nature of the interaction between the molecule and the surface plays an important role in determining the functionality, efficiency, and physical characteristics of the device.[10−14]

In molecular electronics, typically a single molecule (or a small group of ones) bridges the gap between two semi-infinite metallic leads. Hence, the function of the whole device is strongly affected by the exact details of the molecule–lead coupling scheme. Indeed, in recent years it has been shown that the interface between the molecule and the lead is at least as important in determining the transport characteristics of the junction as the electronic properties of the molecular bridge itself.[13−21] Therefore, gaining understanding of the electronic coupling between the molecular core and the contacting leads in such junctions is of fundamental importance for deciphering their transport characteristics and designing structures with desired functionality.

When modeling molecular electronics junctions,[21−23] usually one of the two following equivalent perspectives of the system is adopted: either an atomistic[24−26] or an energy[27,28] representation. In the atomistic representation, the real-space structure of the junction is explicitly considered and the position and identity of all atoms in the model junction uniquely define the corresponding Hamiltonian. This allows one to explore the effects of specific chemical modifications and junction geometry on the transport characteristics and on the function of the suggested device. Nevertheless, if one wishes to explore the nature of the coupling between the eigenstates of the various sections of the system, an energy representation is required. In the energy representation, the junction is formally divided into three sections including the left and right lead regions and the molecule, each region being represented by its corresponding manifold of eigenstates. The states of the molecule are directly coupled to each of the two-lead manifolds, and the interlead couplings are usually neglected. Here, the exact structure and chemical nature of the junction are typically taken into account only implicitly, via a phenomenological model chosen to represent the various energy manifolds and the corresponding coupling matrix elements in the model Hamiltonian.

Because the atomistic and energy perspectives are, in a sense, complementary, they do not provide an obvious route for understanding how chemical interactions translate to coupling between molecular and lead states. Recently, we demonstrated how a simple unitary transformation that we denoted as the "site-to-state" transformation can interconnect these two views, making them rigorously equivalent.[29] Here, we use this transformation in order to gain fundamental insights into the molecule–lead coupling scheme in single-molecule junctions described by an atomistic Hamiltonian. Specifically, we observe the appearance of coupling bands and study the effect of electrode dimensionality and geometry on their nature.

Received: June 29, 2015
Published: September 11, 2015

DOI: 10.1021/acs.jctc.5b00612
J. Chem. Theory Comput. 2015, 11, 4861−4869

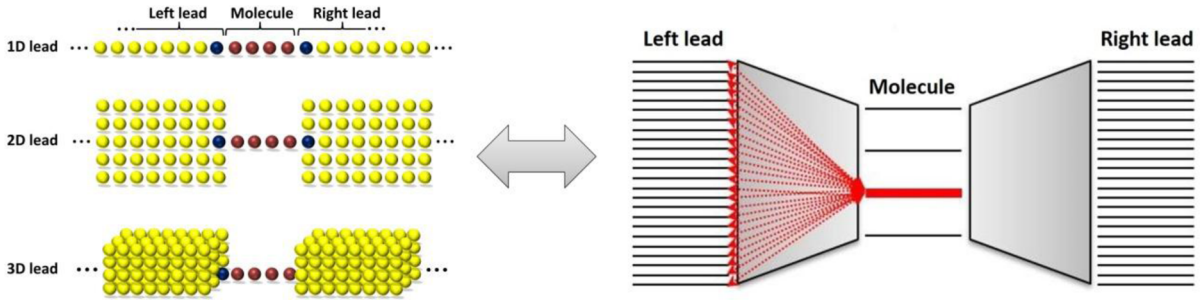

Figure 1. Schematic representation of the site-to-state transformation of a two-lead junction model. Left: Real-space representation of a system with one-dimensional (upper left panel), two-dimensional (middle left panel), and three-dimensional (lower left panel) lead models. Yellow, red, and blue spheres represent sites belonging to the lead, molecule, and coupling regions, respectively. Right: Scheme of the state representation of the junction, where the manifold of eigenstates of the molecule couples separately to the manifolds of eigenstates of the left and right leads. The dashed red lines represent the coupling of the highest occupied molecular orbital of the molecule to the left lead state manifold.

Furthermore, we demonstrate how this concept can shed light on the charge transport behavior of the junction and provide intuition as to the physical processes underlying electron dynamics in open quantum systems.

MODEL

We choose a simple tight-binding (TB) Hamiltonian, represented in real space. This allows us to focus on the basic concepts while avoiding complications arising from more involved electronic structure methods. It should be emphasized, however, that the analysis is, in principle, valid for any single-particle Hamiltonian description of the system. The junction is formally divided into the left (L) and right (R) lead sections and the molecule (M) region (see Figure 1) such that the Hamiltonian matrix representation of the system is of the following form:

$$\hat{H} = \begin{pmatrix} \hat{H}_L & \hat{V}_{L,M} & \hat{0} \\ \hat{V}_{M,L} & \hat{H}_M & \hat{V}_{M,R} \\ \hat{0} & \hat{V}_{R,M} & \hat{H}_R \end{pmatrix} \tag{1}$$

Here, $\hat{H}_I$ is the Hamiltonian matrix block of the Ith section of the system and $\hat{V}_{I,J}$ represents the interactions between sections I and J, where $I, J = (L, M, R)$. In the tight-binding model the interactions are short-ranged and therefore $\hat{V}_{I,J}$ is a sparse matrix, such that we can safely neglect the direct coupling between the leads: $\hat{V}_{L,R} = \hat{V}_{R,L} = 0$.

In order to study the molecule−lead coupling scheme, we transform the real-space site based TB Hamiltonian of eq 1 to the energy representation, in the basis of the eigenstates of the isolated system sections (see Figure 1). To this end, we utilize a site-to-state transformation,[29] where one first separately obtains the diagonal representations of the Hamiltonian blocks corresponding to the individual sections of the system $\hat{\tilde{H}}_I = \hat{U}_I^{\dagger}\hat{H}_I\hat{U}_I$ and their related unitary transformation matrices $\hat{U}_I$. This is followed by the construction of a block-diagonal global unitary transformation matrix of the form

$$\hat{U} = \begin{pmatrix} \hat{U}_L & \hat{0} & \hat{0} \\ \hat{0} & \hat{U}_M & \hat{0} \\ \hat{0} & \hat{0} & \hat{U}_R \end{pmatrix} \tag{2}$$

that transforms the full real-space Hamiltonian matrix representation of eq 1 in the following manner:

$$\hat{\tilde{H}} = \hat{U}^{\dagger}\hat{H}\hat{U} = \begin{pmatrix} \hat{\tilde{H}}_L & \hat{\tilde{V}}_{L,M} & \hat{0} \\ \hat{\tilde{V}}_{M,L} & \hat{\tilde{H}}_M & \hat{\tilde{V}}_{M,R} \\ \hat{0} & \hat{\tilde{V}}_{R,M} & \hat{\tilde{H}}_R \end{pmatrix} \tag{3}$$

Here, $\hat{\tilde{H}}_L$, $\hat{\tilde{H}}_R$, and $\hat{\tilde{H}}_M$ are diagonal square matrices containing the eigenenergies of the isolated left and right leads and molecular sections on their diagonals, respectively, and $\hat{\tilde{V}}_{I,J} \equiv \hat{U}_I^{\dagger}\hat{V}_{I,J}\hat{U}_J$ contains the coupling matrix elements between the eigenstate manifolds of sections $I \neq J$. Note that the fact that we have neglected the direct coupling between the leads in the real-space representation is reflected in the energy representation, as well.

We seek the coupling matrix elements between the bridge molecular orbitals (MOs) and the states of the finite-lead models. These elements are stored, by definition, in the columns (or rows) of the off-diagonal blocks $\hat{\tilde{V}}_{L,M}$ and $\hat{\tilde{V}}_{R,M}$ of the transformed Hamiltonian matrix. As presented in Figure 2,

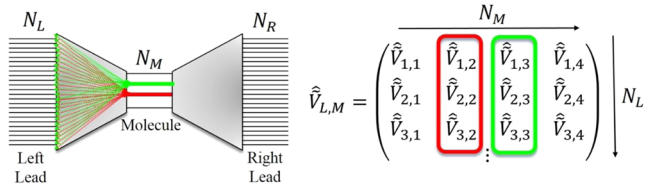

Figure 2. Coupling matrix elements between the molecular bridge MOs and the finite lead model states, as stored in the columns of the off-diagonal block $\hat{\tilde{V}}_{L,M}$ of the transformed Hamiltonian matrix. Red and green lines schematically represent the coupling matrix elements of the highest occupied MO (HOMO) and lowest unoccupied MO (LUMO) levels of a four-site "chain-bridge" molecule, respectively.

the matrix $\hat{\tilde{V}}_{L,M}$ is of the size of $N_L \times N_M$, where N_I is the number of states in section I, and each of the N_M columns represents the coupling of a specific state of the molecule to the left lead state manifold. For a nearest-neighbor tight-binding model simple expressions can be obtained for these interstate coupling terms. To this end, we realize that in the site representation the coupling matrix $\hat{V}_{L,M}$ has only one nonvanishing element, being the hopping term between the

DOI: 10.1021/acs.jctc.5b00612
J. Chem. Theory Comput. 2015, 11, 4861−4869

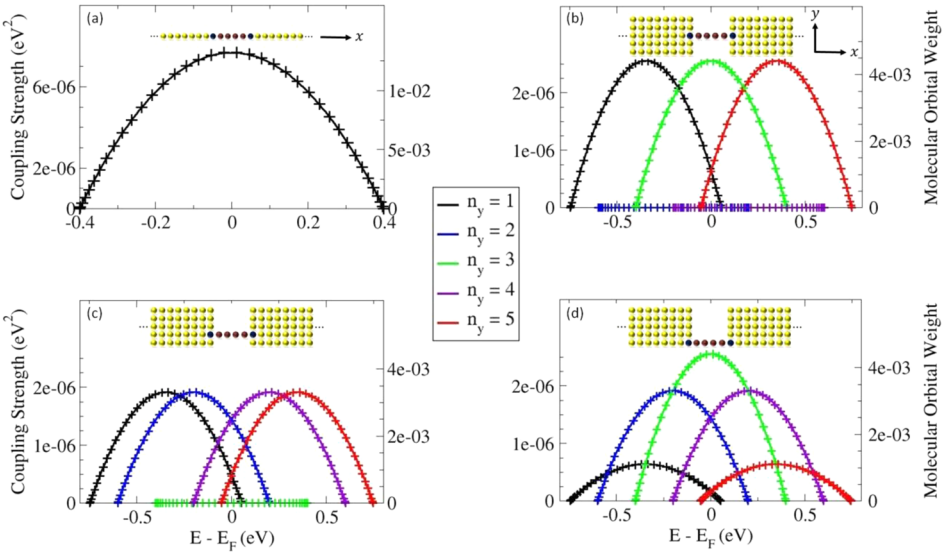

Figure 3. Coupling bands and coupling atom molecular orbital coefficients of a one-dimensional (a) and three two-dimensional (b–d) lead model systems. The absolute square values of the coupling matrix elements between the highest occupied MO of the bridge and the entire manifold of states of the left lead are presented in full lines. The Fermi energy of the lead (E_F) is chosen as the origin of the energy axis. The plus marks represent the weight (absolute square value of the MO coefficient) of the various lead MOs on the edge lead atom directly coupled to the bridge. The coupling values are given by the left *y*-axis, and the lead MO weights are given by the right *y*-axis. In all calculations the on-site energies are taken to be $\alpha_L = \alpha_M = \alpha_R = 0$ eV, the intra-lead and intra-molecule hopping integrals used are $\beta_L = \beta_M = \beta_R = -0.2$ eV, and the lead–molecule hopping terms are $\beta_{L,M} = \beta_{M,R} = -0.04$ eV. For the 1D system the leads are represented by $N_L = N_R = 150$ atom chains, and for the 2D lead models each lead consists of five rows of 150 atoms each, such that $N_L = N_R = 5 \times 150$. In all cases, the molecular bridge consists of $N_M = 4$ sites. The various bands are marked with different colors that represent the perpendicular quantum number of the corresponding lead states n_y (see text for details).

molecule's edge atom and the lead atom to which it is directly coupled. We mark this term as $\beta_{l,m}$, where l and m denote the left lead and molecule coupled sites, respectively. Hence, the coupling between state i of the left lead and state j of the molecule is given by

$$(\hat{V}_{L,M})_{i,j} = (C^{L\dagger})_{i,l}\beta_{l,m}C^{M}_{m,j} \tag{4}$$

where $C^{L}_{l,i}$ is the weight (expansion coefficient) of the lead MO i at the lead atomic site l and, similarly, $C^{M}_{m,j}$ is the weight of the molecule MO j at site m of the molecule. As can be seen, in this simple case, the variation of the coupling between a given molecular state and the various lead states depends solely on the weight of the corresponding lead MOs at the coupling lead site. Hence, these variations reflect an electronic property of the lead. For more general Hamiltonian representations, such as those obtained when using nonorthogonal basis set expansions, the expression for the state couplings will be slightly more involved, such that its dependence on the identity of the molecule and lead states will be dictated by the nature of the real-space coupling model.

Finally, it should be noted that the site-to-state transformation used here is mathematically valid regardless of the molecule–lead coupling strength. Nevertheless, the division of the system into various sections is physically motivated only when the different parts are sufficiently weakly coupled such that each MO of the full system is mainly localized on one of these sections. In this case, the basis of eigenstates of the isolated system sections provides a suitable representation of the problem.

RESULTS

Coupling Bands. Using the formalism described above, we start by examining a one-dimensional (1D) two-lead junction model. Here, the leads are represented by two finite atomic chains bridged by a third finite atomic chain, representing the molecule that is locally coupled to both leads (see inset of Figure 3a). Following the construction of the real-space Hamiltonian matrix representation (with the TB parameters given in the caption of Figure 3) we perform the site-to-state transformation of eq 3.

In Figure 3a, we present the square absolute value of the coupling matrix elements, given by eq 4, as a function of the corresponding lead-state eigenenergy for the case where the index j denotes the highest occupied MO (HOMO) of the molecular bridge and the index i runs over the manifold of states of the left lead (see red lines in the right panel of Figure 1). As can be seen, a clear "coupling band" is formed, with a peak shape centered around the Fermi energy, where the coupling is strongest. We note that when a single atomic site locally interacts with a one-dimensional TB chain consisting of N sites, an analytical expression for the coupling band is obtained within the Anderson–Newns model.[30] In this model, the coupling between the sole atomic state $|a\rangle$ and chain state $|k\rangle$ is given by $V_{a,k} = \beta(2/(N+1))^{1/2}\sin(\pi k/(N+1))$,[31] where β is the hopping integral between the atomic site and the edge chain site and the index k runs over all chain states, $k = 1, 2, ..., N$. When the bridge is longer than a single site, as in Figure 3a, a slightly modified yet very similar band forms.

In order to understand the origin of this coupling band, we recall that according to eq 4 within the TB model the coupling matrix elements between the bridge MOs and the lead states are proportional to the weight of the isolated lead single-particle wave functions at the edge site directly coupled to the bridge (marked in blue in the insets of Figure 3). The latter, which are given by the absolute square values of the isolated lead MO expansion coefficients at the coupling lead site, are plotted as plus marks in Figure 3. Then, a simple scaling by

DOI: 10.1021/acs.jctc.5b00612
J. Chem. Theory Comput. 2015, 11, 4861–4869

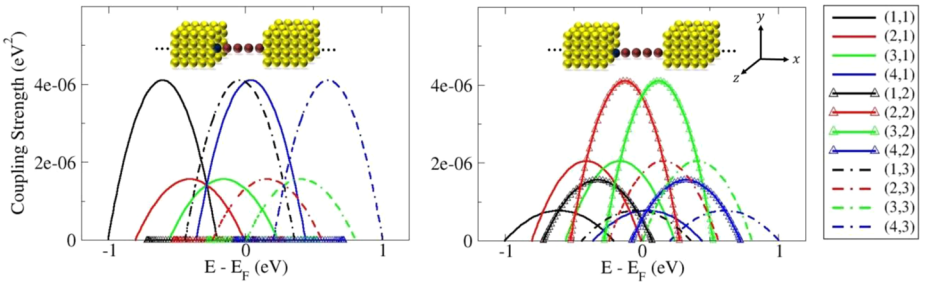

Figure 4. Coupling bands of a TB molecular junction consisting of two 3D leads. The two panels present the couplings between the HOMO state of the molecular bridge and the left lead state manifold for two bridge configurations (see insets). The lead dimensions are $N_x \times N_y \times N_z = 50 \times 3 \times 4$,[35] and the bridge consists of $N_M = 4$ sites. The on-site energies are taken as $\alpha_L = \alpha_M = \alpha_R = 0$ eV, and the intra-lead, intramolecule, and lead−molecule hopping integrals used are $\beta_L = \beta_R = -0.2$ eV, $\beta_M = -0.2$ eV, and $\beta_{L,M} = \beta_{M,R} = -0.04$ eV, respectively. The bands are classified according to the set of perpendicular quantum numbers (n_y,n_z), with appropriately assigned colors.

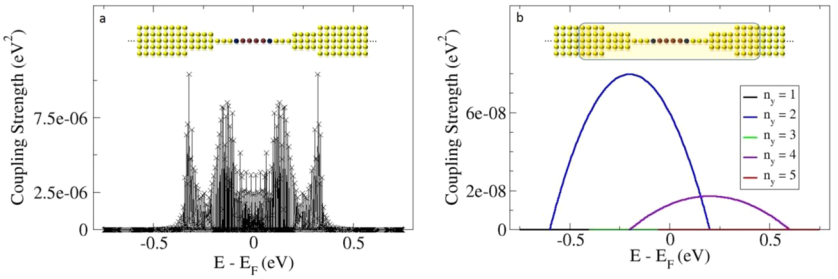

Figure 5. Coupling schemes of a tip-shaped junction model. (a) Coupling scheme of the HOMO level of the four-site tight-binding chain bridge and the manifold of states of a tip-like five-row 2D lead model with 150, 154, and 158 sites in the external, intermediate, and central lead rows, respectively. (b) Coupling scheme of the HOMO level of the "extended molecule", schematically marked by the shaded rectangle, and the manifold of states of the rectangular lead. Here, the extended molecule consists of the four molecular sites and the two adjacent lead sections each of 50, 54, and 58 sites in the external, intermediate, and central lead rows, respectively, and the rectangular leads have five rows of 150 atoms each such that $N_L = N_R = 5 \times 150$. All tight-binding on-site energies are null, the intramolecular and intralead hopping integrals are −0.2 eV, and the lead−molecule hopping integral is −0.04 eV.

$|\beta_{x,m}(C_{m,j})_M|^2$ directly relates the two diagrams. From this it becomes evident that the appearance of the coupling band in this simple TB model can be interpreted as an explicit property of the corresponding lead, as mentioned earlier. Furthermore, only MOs having a significant weight on the lead site that couples to the bridge will have a direct effect on the lifetime of the bridge states.

Next, we consider two-dimensional (2D) lead models. In Figure 3b, the coupling scheme of the bridge HOMO and the left lead eigenstate manifold is plotted for the case where the bridge is located at the center of a five-row finite-lead model. As can be seen, the coupling matrix elements now form three nonvanishing coupling bands, one centered on the Fermi energy and the other two appearing at higher and lower energies, respectively. When the bridge is shifted away from the lead center (Figure 3c), four nonvanishing bands appear, and when the lead is positioned near the edge of the lead model, a fifth nonvanishing coupling band emerges. As for the 1D case, and in agreement with eq 4, regardless of the junction geometry all coupling bands are found to be directly proportional to the weight of the lead MOs on the site directly coupled to the bridge (plus marks in Figure 3).

The appearance of several coupling bands for the 2D leads setup can be rationalized via simple particle-in-a-box arguments. The TB MOs of the isolated 2D lead models follow the symmetry of the wave functions of a single-particle confined to a 2D box:[32] $\psi_{n_x,n_y}(x,y) = (2/L_x)^{1/2}(2/L_y)^{1/2}\sin(n_x\pi x/L_x)\sin(n_y\pi y/L_y)$. Here, $L_i = (N_i + 1)a_i$ are the dimensions of the box along the junction's main axis ($i = x$) and perpendicular to it ($i = y$), N_i and a_i are the corresponding number of lead sites and intersite distances, respectively, and n_x, n_y are the two quantum numbers. Within the TB model, the quantum numbers can obtain the values $n_x = 1, 2, ..., N_x$ and $n_y = 1, 2, ..., N_y$. For a fixed value of n_y, the weight of the various axial MOs at the lead edge atoms facing the bridge form a band similar to that obtained in the 1D lead case (Figure 3a). The different bands, then, correspond to different quantum numbers n_y. Because our 2D lead model is constructed of $N_y = 5$ rows, we expect to find five coupling bands in this case. Nevertheless, because the perpendicular component of the wave function, $\sin(n_y\pi y/L_y)$, has nodes at the center of the lead cross-section for $n_y = 2, 4$, the corresponding two bands vanish, as evident in Figure 3b.[33] When the bridge is connected to the second lead row (Figure 3c), $n_y = 3$ produces a node at this position in the perpendicular wave function and the corresponding coupling band vanishes. For the case depicted in Figure 3d, all five bands appear and their relative height is determined by the weight of the perpendicular wave component on the corresponding lead-bridge coupling site.

We can therefore classify the various coupling bands according to the corresponding perpendicular quantum number. The exact expression for the eigenenergies of the different 2D lead MOs is given by the following tight-binding expression:[32,34] $E_n = \alpha + 2\beta[\cos(\pi n_x/(N_x+1)) + \cos(\pi n_y/(N_y+1))]$ where α is the on-site energy and β the nearest-neighbors hopping integral, both assumed to be uniform within the lead model. Using this expression, we associate each point in the different diagrams of Figure 3 with the corresponding

DOI: 10.1021/acs.jctc.5b00612
J. Chem. Theory Comput. 2015, 11, 4861−4869

lead state and assign a color to it according to the value of its perpendicular quantum number. This clearly demonstrates that indeed each coupling band corresponds to a different value of n_y.

The same type of analysis can be applied to the case of three-dimensional (3D) leads. In Figure 4, we present the coupling bands for a junction consisting of 3D lead models with two bridge configurations (see insets). For clarity of presentation, the corresponding MO weights are omitted. Similar to the case of lower dimensional leads, the coupling bands are found to be proportional to the weights of the lead MOs on the coupling lead site and can be classified according to the set of perpendicular quantum numbers (n_y,n_z), using the corresponding energy expression $E_n = \alpha + 2\beta[\cos(\pi n_x/(N_x + 1)) + \cos(\pi n_y/(N_y + 1)) + \cos(\pi n_z/(N_z + 1))]$. The total number of coupling bands in this case is $N_y \cdot N_z$ which, for our lead model, amounts to 12. The relative peak intensities of the coupling bands depend on the location of the bridge with respect to the lead surface, with vanishing bands resulting from nodes of the perpendicular lead MOs (see left panel of Figure 4).

More Complex Molecule–Lead Interfaces. In the systems discussed above we have used simple cubic lead models that produced distinct coupling bands, which could be readily associated with the different quantum numbers characterizing the various lead states. Because the structure of these bands was shown to be a property of the leads within the TB model, one may expect a richer behavior if the molecule–lead interface is more complex. To demonstrate this, we present in Figure 5a the coupling scheme between the HOMO level of a four-site tight-binding chain bridge and the manifold of states of a tip-like 2D lead model. In this geometry, it is much more difficult to assign different coupling bands to simple quantum numbers of various subgroups of lead states. Nevertheless, the appearance of coupling bands is still noticeable.

We note that for the same junction one could, in principle, define an "extended molecule", which includes the molecule augmented by its adjacent lead sections (see the shaded rectangle in the inset of Figure 5b), and study the coupling between its states and the manifold of cubic lead states. Due to the resemblance of the lead structures, this results in a simple coupling band scheme (see Figure 5b) similar to that shown in Figure 3. However, while mathematically valid, this would not be useful for studying the effects of the molecule–lead coupling scheme on the transport properties of the junction. Furthermore, as stated earlier, since the virtual interface in this case separates two strongly coupled sections, the physical relevance of this representation is limited. Hence, when performing the virtual division of the system into sections, the location of the various interfaces should vary according to the specific application. In transport calculations it is important to minimize the effect of the scattering region on the electronic properties of the semi-infinite-lead models. Therefore, an extended molecule approach is useful. However, when studying the coupling scheme within the scattering region, the virtual interface of interest should be positioned between the "bare" molecule and the full lead model.

Relation to Electronic Transport. The coupling bands discussed previously provide a different perspective to the overall molecule–lead coupling scheme, which, in turn, is of key importance (along with the electronic structure of the bridge itself) in determining the electronic transport properties of the junction. They may thus be used to investigate the effect of junction chemistry, geometry, and dimensionality on the transport characteristics of the system. Here, it is important to consider the collective effect of the full coupling band. This is because when using finite-lead models,[24,36] the individual coupling strength between a specific bridge state and one lead level generally depends on the lead size.[34] Specifically, the normalization requirement of the isolated lead MOs dictates a general reduction of its weight on the lead–bridge coupling site with increasing lead size and hence a corresponding decrease in the individual coupling strengths (see Figure 6). Naturally, this

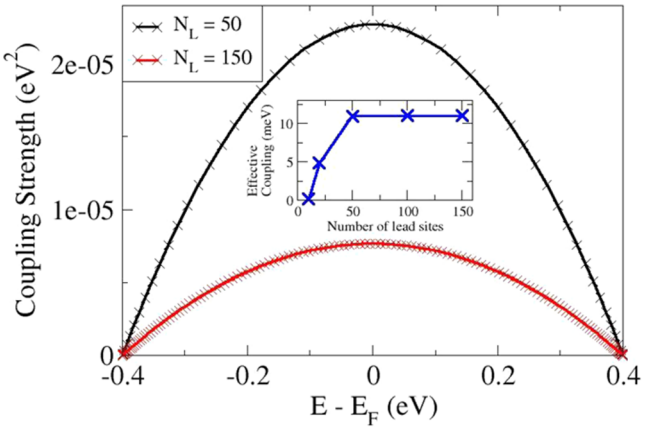

Figure 6. Coupling scheme of the HOMO level of a four-site tight-binding chain bridge and the manifold of states of a one-dimensional lead model. The black and red curves represent a system with lead size of $N_L = N_R = 50$ and $N_L = N_R = 150$ atoms chains, respectively. In all cases, the on-site energies are taken to be $\alpha_L = \alpha_M = \alpha_R = 0$ eV and the intralead, intramolecule, and lead–molecule hopping integrals used are $\beta_L = \beta_R = -0.2$ eV, $\beta_M = -0.2$ eV, and $\beta_{L,M} = \beta_{M,R} = -0.04$ eV, respectively. Inset: The overall lead–molecule effective coupling as a function of the lead size, computed using eq 5 over the HOMO and LUMO molecular states. Here, since the eigenvalue spectrum of the finite-lead models is discrete, we broaden the δ functions appearing in eq 5 by convolving them with a Gaussian of width 0.013 eV regardless of the lead model size. This value corresponds to the typical eigenvalue spacing near the Fermi energy of the 100-site lead model with the same TB parameters and to the driving rate for which the Landauer steady state current is recovered in the driven Liouville von Neumann calculation (see eq 6) using 150-site lead models.

is compensated for by the appearance of new lead states in the coupling band, and hence the overall lead–molecule coupling is expected to converge for sufficiently large finite-lead models.

To demonstrate this, we use the Fermi golden rule definition of the effective coupling between any bridge state and the full lead manifold of states as follows:[37]

$$\Gamma_{L/R}(\varepsilon_n) = 2\pi \sum_q |V_{n,q}^{L/R}|^2 \delta(\varepsilon_n - \varepsilon_q^{L/R}) \tag{5}$$

Here, $V_{n,q}^{L/R}$ are the coupling matrix elements between a bridge state of energy ε_n and a state of energy $\varepsilon_q^{L/R}$ of the left or right lead, and the sum runs over all states in the relevant lead manifold. We can then define the overall effective lead–molecule coupling as the sum of all bridge–state couplings relevant for transport, i.e., $\Gamma_{L/R} = \sum_n \Gamma_{L/R}(\varepsilon_n)$ where n is an index for the pertinent bridge energy levels. As can be seen in the inset of Figure 6, the calculated effective lead–molecule coupling converges rapidly with the size of the lead model, such that tripling the lead size from 50 to 150 sites results in reduction of the individual coupling strengths by a factor of 3,

DOI: 10.1021/acs.jctc.5b00612
J. Chem. Theory Comput. 2015, 11, 4861–4869

and hence the overall lead−molecule effective coupling remains unaffected.

We expect the steady-state current flowing through the bridge to be proportional to its effective coupling to the leads. To validate this, we examine the three system configurations depicted in the insets of Figure 3b−d, consisting of 2D lead structures bridged by an atomic chain. First, we calculate the transport properties of these three junction configurations using our recently suggested driven Liouville von Neumann approach[29] that was shown to accurately describe electron dynamics in metal−molecule−metal junctions under the influence of time-dependent driving forces.[37] Here, the time-dependent bond current between sites n and $n+1$ is calculated via $I_{n,n+1}(t) = (2\beta e/\hbar)\ \mathrm{Im}[\rho_{n,n+1}(t)]$, where e is the electron charge, $\hbar$ is the reduced Planck constant, β is the hopping matrix element between the two sites, and $\rho_{n,n+1}(t)$ is the instantaneous off-diagonal element of the density matrix representing the relevant site coherences.[29,38] The dynamics of the density matrix $\hat{\rho}(t)$ of the system, whose electronic properties are given by the Hamiltonian $\hat{H}$, is calculated via the driven Liouville von Neumann equation:

$$\frac{\mathrm{d}}{\mathrm{d}t}\hat{\rho}(t) = -\frac{i}{\hbar}[\hat{H}, \hat{\rho}(t)] - \Gamma\begin{pmatrix} \hat{\rho}_L(t) - \hat{\rho}_L^0 & \frac{1}{2}\hat{\rho}_{L,M}(t) & \hat{\rho}_{L,R}(t) \\ \frac{1}{2}\hat{\rho}_{M,L}(t) & \hat{0} & \frac{1}{2}\hat{\rho}_{M,R}(t) \\ \hat{\rho}_{R,L}(t) & \frac{1}{2}\hat{\rho}_{R,M}(t) & \hat{\rho}_R(t) - \hat{\rho}_R^0 \end{pmatrix} \quad (6)$$

The first term on the right-hand side of eq 6 provides the standard unitary dynamics whereas the second term introduces source and sink terms that impose the appropriate boundary conditions, effectively opening the finite closed model system. The sink term consists of the various $\hat{\rho}_{i,j}(t)$ density matrix blocks corresponding to the left (L), molecule (M), and right (R) sections of the system. The source term includes the target density matrix diagonal blocks, $\hat{\rho}^0_{L/R}$, encoding the equilibrium Fermi−Dirac distribution with the corresponding chemical potential and electronic temperature of each lead. The driving rate, Γ, can be deduced from the typical time scale for electron reflection from the boundaries of the finite model system and fine-tuned to reproduce the Landauer steady-state current values.[29]

In Figure 7, we present the time-dependent bond current at the bridge center of the three junctions depicted in Figure 3b−d. In all calculations we use a driving rate of $\Gamma = 0.0075$ fs^{-1} chosen to reproduce the Landauer steady-state currents for these systems. As can be seen, the specific junction geometry has considerable influence on the resulting steady-state currents. The steady-state current obtained when the bridging molecule is at (Figure 3b) or immediately off (Figure 3c) the center of the lead is similar (but not identical): 1.55 and 1.57 μA, respectively. However, the current obtained when the bridging molecule is at the edge of the lead (Figure 3d) is appreciably larger, 2.03 μA.

Next, we use eq 5 to calculate the effective coupling of the bridge to the leads using a Gaussian broadening of $\sigma = 0.0049$ eV for the discrete lead eigenspectrum, for all three systems considered. This broadening was chosen to relate to the earlier-

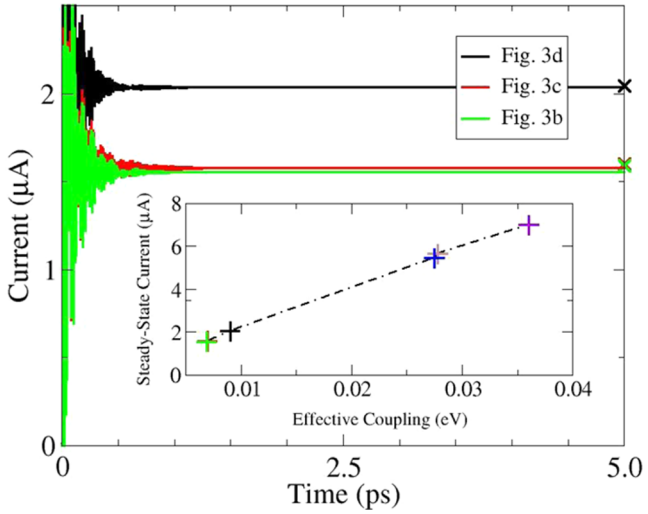

Figure 7. Current as a function of time for the system configurations depicted in Figure 3b−d, under a bias voltage of $V_b = 0.3$ V, electronic lead temperatures of $T_L = T_R = 0$ K, and a driving rate of $\Gamma = 0.0075$ fs^{-1}. In all calculations the on-site energies are taken to be $\alpha_L = \alpha_M = \alpha_R = 0$ eV and the hopping integrals used are $\beta_L = \beta_M = \beta_R = -0.2$ eV and $\beta_{L,M} = \beta_{M,R} = -0.04$ eV. Colored × marks designate the corresponding steady-state currents calculated via the Landauer formalism (for more details see ref 29). A time step of 1.0 fs is used throughout the simulations. Inset: steady-state current vs the effective coupling calculated using only the HOMO and LUMO levels that reside within the Fermi transport window. Green, red, and black plus signs designate the steady-state currents obtained for the configurations depicted in Figure 3b−d, respectively, using the same parameters as in the main panel. Blue, brown, and violet plus signs designate the steady-state currents obtained for the configurations depicted in Figure 3b−d, respectively, but with increased lead−molecule hopping integrals of $\beta_{LM} = \beta_{MR} = -0.08$ eV.

stated driving rate, Γ, via $\sigma = \hbar\Gamma$ (we note that a more rigorous way to extract state-dependent broadening factors has been recently suggested in ref 39). The resulting effective couplings of the three configurations are 6.87, 6.94, and 9.01 meV, for configurations 3b, 3c, and 3d, respectively, where in eq 5 we sum over the bridge states residing within the relevant Fermi transport window, determined by the bias voltage and lead electronic temperature. Indeed, this order matches the ordering of the steady-state currents. This is shown explicitly in the inset of Figure 7, where the steady-state current, plotted against the calculated effective coupling, exhibits a monotonic behavior. This demonstrates that the molecule−lead coupling scheme can serve as a tool for rationalizing the transport characteristics of molecular electronic systems and for designing junctions with desired functionality.

Choice of Finite-Lead Models. As discussed previously, within our TB model the appearance of coupling bands results from the electronic structure of the leads. Before concluding, then, we should examine whether the choice of the finite-lead model often used in practice is sufficient to reflect the correct molecule−lead coupling and therefore transport characteristics. This is of particular importance when using a closed system approach, namely, one based on microcanonical calculations,[24,25,40−42] to study the coupling scheme and transport characteristics with finite model systems. Specifically, in addition to the choice of lead material, geometry, and level of underlying electronic structure theory, it is important to verify that the electronic properties of the finite lead converge to

DOI: 10.1021/acs.jctc.5b00612
J. Chem. Theory Comput. 2015, 11, 4861−4869

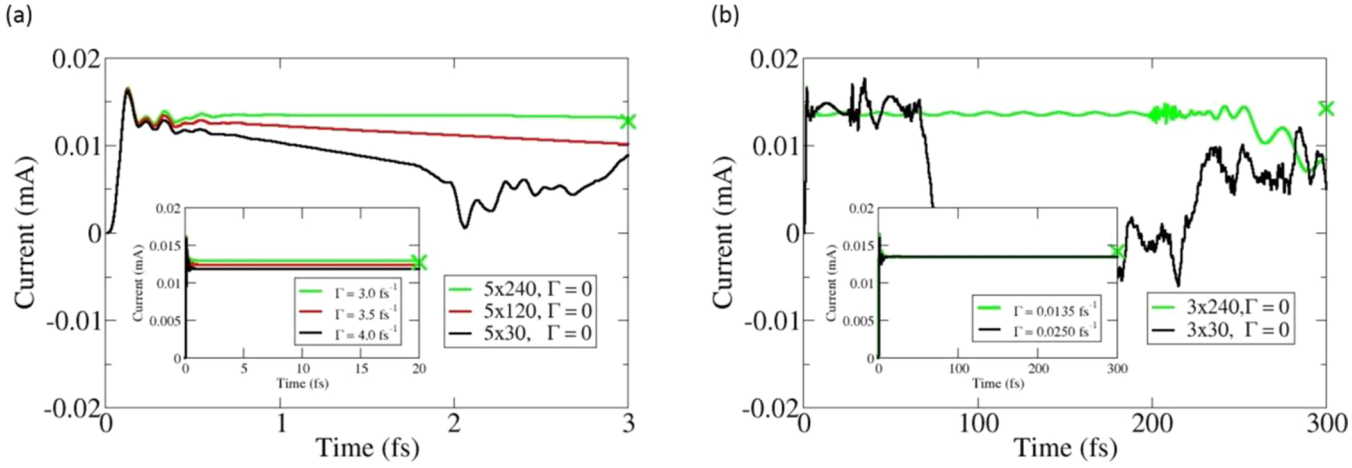

Figure 8. (a) Current as a function of time, calculated at the center of a four-site atomic chain bridging two 2D leads, modeled by finite-lead sections of increasing size using the microcanonical approach. Black, red, and green curves represent results calculated for 2D lead models with five rows consisting of 30, 120, and 240 sites each, respectively. The TB parameters of Ercan and Anderson[44] are adopted, with on-site energies of $\alpha_L = \alpha_M = \alpha_R = 0$ eV and uniform nearest-neighbors hopping integrals of $\beta_L = \beta_M = \beta_R = \beta_{L,M} = \beta_{M,R} = -11.0$ eV throughout the junction. The inset represents results obtained using the driven Liouville von Neumann, eq 6, with driving rates of $\Gamma = 4.0$, 3.5, and 3.0 fs^{-1} for the black, red, and green curves, respectively. (b) Same as panel a, but with 2D lead models of three rows consisting of 30 or 240 atoms each and uniform hopping integrals of $\beta_L = \beta_M = \beta_R = \beta_{L,M} = \beta_{M,R} = -0.8$ eV throughout the junction. The driving rates used in the inset are $\Gamma = 0.025$ and 0.0125 fs^{-1} for the black and green curves, respectively. All results were obtained under a bias voltage of $V_b = 0.2$ V. Green × marks represent the steady-state currents obtained using the Landauer formalism for each case.

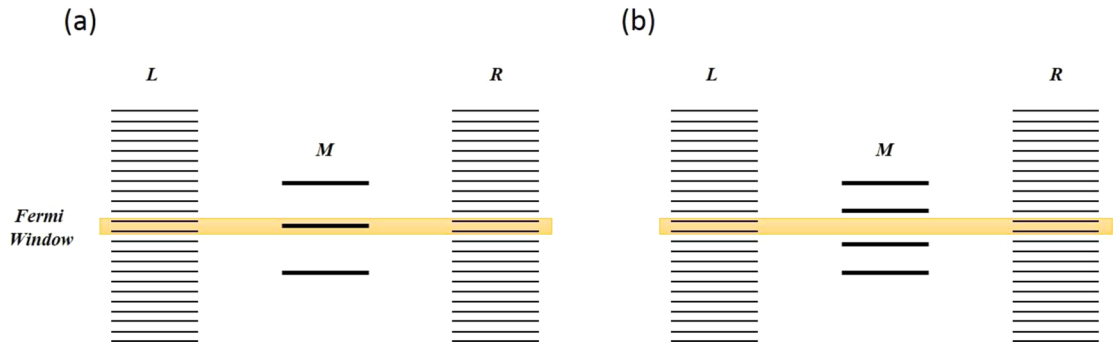

Figure 9. Schematic illustration of the level diagram of a junction consisting of two 2D leads and a molecular chain bridge with odd (a) and even (b) numbers of sites.

those of its semi-infinite counterpart.[34,43] To this end, one has to choose sufficiently large lead sections so as to obtain a reliable description of the density of states within the Fermi transport window in the vicinity of the Fermi energy and a converged effective molecule−lead coupling strength. Most importantly, the appropriate lead model size depends on the electronic character of the molecular bridge itself and can vary if transport is dominated by resonant or tunneling regimes. Here, the site-to-state transformation may provide valuable information regarding the electronic structure and coupling scheme of the junction that, in turn, can be used to determine the required lead model size.

To demonstrate this, we refer to the work of Ercan and Anderson,[44] where it has been reported that the appearance of a quasi-steady-state (QSS) in microcanonical transport calculations[24,25] of closed systems strongly depends on the choice of finite lead model dimensions and the molecular bridge length. In this study, it was numerically demonstrated that for junctions consisting of 2D and 3D lead models bridged by an atomic chain, a QSS is obtained only when the bridge has an odd number of sites. For an even atomic chain bridge, no apparent QSS was observed for the same finite lead model size. Nevertheless, in the limit of (semi)infinite-lead models, the microcanonical approach converges to the full open system description and should produce the correct steady-state current. Hence, one would expect to obtain a clear QSS for sufficiently large, yet finite, lead models also for an even atomic chain bridge.

To verify this, we present in Figure 8a the dependence of the early current dynamics on the finite lead model size in a microcanonical simulation of a junction consisting of a four-site bridge and 2D leads. For lead models that consist of five atomic rows, each 30 atoms long, we reproduce the results of Ercan and Anderson[44] (black curve in Figure 8a). As the length of the lead is increased to 120 and 240 sites (red and green curves in Figure 8a, respectively); however, an apparent quasi-steady-state develops for the even bridge chain as well. This suggests that a larger finite-lead model with a higher DOS within the Fermi transport window in the vicinity of the Fermi energy is required to provide a reliable description of the current dynamics in the microcanonical calculation of the even bridge chain, as compared to the odd chain. Reducing the value of the

DOI: 10.1021/acs.jctc.5b00612
J. Chem. Theory Comput. 2015, 11, 4861−4869

hopping integral decreases the lead bandwidth and hence increases its overall DOS. As a result (see Figure 8b) a fairly stable QSS appears in the even bridge case already for the 30-site-long lead models (black curve), with considerable improvement upon extending the lead lengths to 240 sites. It should be noted that, for all cases presented in Figure 8, even when a microcanonical QSS could not be reached, the driven Liouville von Neumann eq 6,[29] with appropriate driving rates, produces a stable steady state whose value corresponds well to the Landauer result[45] (see insets of Figure 8).

To rationalize the difference in convergence of the microcanonical QSS behavior with respect to the lead size for even and odd numbers of bridge chain sites, we schematically plot the level diagram of the junction for the two cases in Figure 9. For the odd bridge case (Figure 9a) there is a molecular level situated at the center of the Fermi transport window[46] leading to resonant transport that requires a fair density of lead states at the Fermi energy in order to mimic the infinite-lead case. For the even bridge case (Figure 9b) a molecular HOMO−LUMO gap of 0.25 eV opens around the lead Fermi energy for the chosen parameters. Here, transport is governed by off-resonance transmission throughout the Fermi transport window. This, in turn, requires a much higher density of lead states to capture the low current dynamics and therefore is more demanding of the finite-lead model.[47] This example thus demonstrates that a site-to-state transformation, which provides direct access to the electronic structure of the molecular bridge, the leads, and the nature of their coupling, is an effective tool in designing finite-lead models that will produce converged transport results.

SUMMARY AND CONCLUSIONS

The interface between a molecule and the surface of a semi-infinite lead plays a decisive role in determining the transport properties of molecular electronic devices. By transforming between an atomistic view of the junction and a state representation, where the couplings between the eigenstates of the various isolated sections of the full system are obtained explicitly, we were able to gain a fundamental understanding of the overall coupling scheme and to evaluate its effect on the time-dependent current passing through the system. We found coupling bands that correspond to the lead molecular orbitals weight at the lead−molecule coupling site and depend on the dimension and shape of the lead and the overall junction geometry. Finally, we have demonstrated the sensitivity of computational transport methodologies that avoid the use of semi-infinite leads to the choice of finite lead model size and showed how the transformation from the real-space to the energy representation of the junction may help rationalizing this choice. Specifically, we demonstrated how this concept can shed light on the charge transport behavior of the junction and provide intuition as to the physical processes underlying electron dynamics in open quantum systems.

AUTHOR INFORMATION

Corresponding Author

*E-mail: odedhod@tau.ac.il.

Funding

Work at TAU was supported by the German-Israeli Foundation under research Grant No. 2291-2259.5/2011, the Israel Science Foundation under Grant No. 1740/13, the Lise-Meitner Minerva Center for Computational Quantum Chemistry, and the Center for Nanoscience and Nanotechnology at Tel-Aviv University. Work at Weizmann was supported by the Israel Science Foundation and the Lise-Meitner Minerva Center for Computational Quantum Chemistry.

Notes

The authors declare no competing financial interest.

ACKNOWLEDGMENTS

We thank Prof. Abraham Nitzan and Prof. Tamar Seideman for many helpful discussions and Prof. Matthew G. Reuter for providing his valuable remarks on the manuscript.

REFERENCES

(1) Kirubakaran, A.; Jain, S.; Nema, R. K. A review on fuel cell technologies and power electronic interface. *Renewable Sustainable Energy Rev.* **2009**, *13*, 2430−2440.
(2) *Fuel Cell Catalysis: A Surface Science Approach*; Koper, M. T. M., Ed.; John Wiley & Sons: Hoboken, NJ, USA, 2009.
(3) Brabec, C. J. Organic photovoltaics: technology and market. *Sol. Energy Mater. Sol. Cells* **2004**, *83*, 273−292.
(4) Brédas, J. L.; Norton, J. E.; Cornil, J.; Coropceanu, V. Molecular Understanding of Organic Solar Cells: The Challenges. *Acc. Chem. Res.* **2009**, *42*, 1691−1699.
(5) Lin, Y.; Zhan, X.: Organic Solar Cells Based on Small Molecules In *Organic Optoelectronics*; Hu, W., Ed.; Wiley-VCH Verlag GmbH: Weinheim, Germany, 2013.
(6) Kushmerick, J. G. Metal-molecule contacts. *Mater. Today* **2005**, *8*, 26−30.
(7) Cahen, D.; Kahn, A.; Umbach, E. Energetics of molecular interfaces. *Mater. Today* **2005**, *8*, 32−41.
(8) Aradhya, S. V.; Venkataraman, L. Single-molecule junctions beyond electronic transport. *Nat. Nanotechnol.* **2013**, *8*, 399−410.
(9) Bergfield, J. P.; Ratner, M. A. Forty years of molecular electronics: Non-equilibrium heat and charge transport at the nanoscale. *Phys. Status Solidi B* **2013**, *250*, 2249−2266.
(10) Cahen, D.; Kahn, A. Electron energetics at surfaces and interfaces: Concepts and experiments. *Adv. Mater.* **2003**, *15*, 271−277.
(11) Hwang, J.; Wan, A.; Kahn, A. Energetics of metal-organic interfaces: New experiments and assessment of the field. *Mater. Sci. Eng., R* **2009**, *64*, 1−31.
(12) Kronik, L.; Koch, N. Electronic Properties of Organic-Based Interfaces. *MRS Bull.* **2010**, *35*, 417−419.
(13) Jia, C. C.; Guo, X. F. Molecule-electrode interfaces in molecular electronic devices. *Chem. Soc. Rev.* **2013**, *42*, 5642−5660.
(14) The Molecule-Metal Interface. Koch, N., Ueno, N., Wee, A. T. S., Eds. Wiley-VCH Verlag GmbH: Weinheim, Germany, 2013.
(15) Yaliraki, S. N.; Ratner, M. A. Molecule-interface coupling effects on electronic transport in molecular wires. *J. Chem. Phys.* **1998**, *109*, 5036−5043.
(16) Stadler, R.; Jacobsen, K. W. Fermi level alignment in molecular nanojunctions and its relation to charge transfer. *Phys. Rev. B: Condens. Matter Mater. Phys.* **2006**, *74*, 161405−161408.
(17) Tarakeshwar, P.; Palacios, J. J.; Kim, D. M. Electrode-Molecule Interface Effects on Molecular Conductance. *IEEE Trans. Nanotechnol.* **2009**, *8*, 16−21.
(18) Meisner, J. S.; Ahn, S.; Aradhya, S. V.; Krikorian, M.; Parameswaran, R.; Steigerwald, M.; Venkataraman, L.; Nuckolls, C. Importance of Direct Metal-pi Coupling in Electronic Transport Through Conjugated Single-Molecule Junctions. *J. Am. Chem. Soc.* **2012**, *134*, 20440−20445.
(19) Kiguchi, M.; Tal, O.; Wohlthat, S.; Pauly, F.; Krieger, M.; Djukic, D.; Cuevas, J. C.; van Ruitenbeek, J. M. Highly conductive molecular junctions based on direct binding of benzene to platinum electrodes. *Phys. Rev. Lett.* **2008**, *101*, 046801−046804.
(20) Yelin, T.; Vardimon, R.; Kuritz, N.; Korytar, R.; Bagrets, A.; Evers, F.; Kronik, L.; Tal, O. Atomically Wired Molecular Junctions:

DOI: 10.1021/acs.jctc.5b00612
J. Chem. Theory Comput. 2015, 11, 4861−4869

Connecting a Single Organic Molecule by Chains of Metal Atoms. *Nano Lett.* **2013**, *13*, 1956−1961.
(21) McCreery, R. L.; Yan, H. J.; Bergren, A. J. A critical perspective on molecular electronic junctions: there is plenty of room in the middle. *Phys. Chem. Chem. Phys.* **2013**, *15*, 1065−1081.
(22) Xue, Y. Q.; Ratner, M. A. Theoretical principles of single-molecule electronics: A chemical and mesoscopic view. *Int. J. Quantum Chem.* **2005**, *102*, 911−924.
(23) Tao, N. J. Electron transport in molecular junctions. *Nat. Nanotechnol.* **2006**, *1*, 173−181.
(24) Di Ventra, M.; Todorov, T. N. Transport in nanoscale systems: the microcanonical versus grand-canonical picture. *J. Phys.: Condens. Matter* **2004**, *16*, 8025−8034.
(25) Bushong, N.; Sai, N.; Di Ventra, M. Approach to steady-state transport in nanoscale conductors. *Nano Lett.* **2005**, *5*, 2569−2572.
(26) Sanchez, C. G.; Stamenova, M.; Sanvito, S.; Bowler, D. R.; Horsfield, A. P.; Todorov, T. N. Molecular conduction: Do time-dependent simulations tell you more than the Landauer approach? *J. Chem. Phys.* **2006**, *124*, 214708−214714.
(27) Segal, D.; Nitzan, A.; Davis, W. B.; Wasielewski, M. R.; Ratner, M. A. Electron transfer rates in bridged molecular systems 2. A steady-state analysis of coherent tunneling and thermal transitions. *J. Phys. Chem. B* **2000**, *104*, 3817−3829.
(28) Subotnik, J. E.; Hansen, T.; Ratner, M. A.; Nitzan, A. Nonequilibrium steady state transport via the reduced density matrix operator. *J. Chem. Phys.* **2009**, *130*, 144105−144116.
(29) Zelovich, T.; Kronik, L.; Hod, O. State Representation Approach for Atomistic Time-Dependent Transport Calculations in Molecular Junctions. *J. Chem. Theory Comput.* **2014**, *10*, 2927−2941.
(30) Newns, D. M. Self-Consistent Model of Hydrogen Chemisorption. *Phys. Rev.* **1969**, *178*, 1123−1135.
(31) Peskin, U. An introduction to the formulation of steady-state transport through molecular junctions. *J. Phys. B: At., Mol. Opt. Phys.* **2010**, *43*, 153001.
(32) Narioka, S.; Ishii, H.; Edamatsu, K.; Kamiya, K.; Hasegawa, S.; Ohta, T.; Ueno, N.; Seki, K. Angle-Resolved Photoelectron Spectroscopic Study of Oriented P-Sexiphenyl - Wave-Number Conservation and Blurring in a Short Model-Compound of Poly(P-Phenylene). *Phys. Rev. B: Condens. Matter Mater. Phys.* **1995**, *52*, 2362−2373.
(33) Reuter, M. G.; Seideman, T.; Ratner, M. A. Guidelines for choosing molecular "alligator clip" binding motifs in electron transport devices. *J. Chem. Phys.* **2011**, *134*, 154708.
(34) Reuter, M. G. Closed-form Green functions, surface effects, and the importance of dimensionality in tight-binding metals. *J. Chem. Phys.* **2010**, *133*, 034703−034712.
(35) We deliberately choose ny different from nz in order to reduce the junction symmetry and avoid degeneracies that can make the band assignment more difficult.
(36) Evans, J. S.; Van Voorhis, T. Dynamic Current Suppression and Gate Voltage Response in Metal-Molecule-Metal Junctions. *Nano Lett.* **2009**, *9*, 2671−2675.
(37) Chen, L. P.; Hansen, T.; Franco, I. Simple and Accurate Method for Time-Dependent Transport along Nanoscale Junctions. *J. Phys. Chem. C* **2014**, *118*, 20009−20017.
(38) Rai, D.; Hod, O.; Nitzan, A. Circular Currents in Molecular Wires. *J. Phys. Chem. C* **2010**, *114*, 20583−20594.
(39) Liu, Z. F.; Neaton, J. B. Communication: Energy-dependent resonance broadening in symmetric and asymmetric molecular junctions from an ab initio non-equilibrium Green's function approach. *J. Chem. Phys.* **2014**, *141*, 131104−131108.
(40) Cheng, C.-L.; Evans, J. S.; Van Voorhis, T. Simulating molecular conductance using real-time density functional theory. *Phys. Rev. B: Condens. Matter Mater. Phys.* **2006**, *74*, 155112.
(41) Evans, J. S.; Cheng, C.-L.; Van Voorhis, T. Spin-charge separation in molecular wire conductance simulations. *Phys. Rev. B: Condens. Matter Mater. Phys.* **2008**, *78*, 165108.
(42) Evans, J. S.; Voorhis, T. V. Dynamic Current Suppression and Gate Voltage Response in Metal−Molecule−Metal Junctions. *Nano Lett.* **2009**, *9*, 2671−2675.
(43) Reuter, M. G.; Boffi, N. M.; Ratner, M. A.; Seideman, T. The role of dimensionality in the decay of surface effects. *J. Chem. Phys.* **2013**, *138*, 084707.
(44) Ercan, I.; Anderson, N. G. Tight-binding implementation of the microcanonical approach to transport in nanoscale conductors: Generalization and analysis. *J. Appl. Phys.* **2010**, *107*, 124318−124330.
(45) Here, we use the microcanonical boundary conditions driving the edge densities toward the initial charge separated state obtained by applying an external electric field.
(46) Pedersen, K. G. L.; Strange, M.; Leijnse, M.; Hedegard, P.; Solomon, G. C.; Paaske, J. Quantum interference in off-resonant transport through single molecules. *Phys. Rev. B: Condens. Matter Mater. Phys.* **2014**, *90*, 125413−125423.
(47) We note that for sufficiently long molecular chains the density of molecular states converges and transport becomes independent of the chain model parity.

DOI: 10.1021/acs.jctc.5b00612
J. Chem. Theory Comput. 2015, 11, 4861−4869